EPR and ENDOR analysis of Fe^{3+} impurity centers in fluoroelpasolite lattices

Frank Loncke,[a] Hendrik De Cooman,[a] Nicholas M. Khaidukov,[b] Henk Vrielinck,[a] Etienne Goovaerts,[c] Paul Matthys[a] and Freddy Callens*[a]

Received 23rd March 2007, Accepted 20th June 2007
First published as an Advance Article on the web 17th July 2007
DOI: 10.1039/b704406b

Fe^{3+} ions in hexagonal and cubic fluoroelpasolite crystals ($A^I_2B^IM^{III}F_6$) have been investigated in a combined Electron Paramagnetic Resonance (EPR) and Electron Nuclear Double Resonance (ENDOR) study. A detailed analysis of the ENDOR spectra for the nearest ^{19}F and ^{23}Na shells in X (9.5 GHz) and Q band (34 GHz) allowed the complex EPR spectra to be disentangled and to determine the spin Hamiltonian parameters for the various $S = 5/2$ Fe^{3+} centres. W-band (95 GHz) EPR measurements as a function of temperature were performed to provide unambiguous evidence about the absolute signs of the Zero Field Splitting (ZFS) and SuperHyperFine (SHF) parameters for Fe^{3+} in Cs_2NaAlF_6 as already determined from the ENDOR work. It could be concluded that all principal ^{19}F hyperfine values were positive, in agreement with earlier assignments in the literature for related systems. A comparative analysis of the ^{19}F SHF data for Fe^{3+} at a perfectly octahedral site in the cubic crystal, and at two slightly trigonally distorted environments in the hexagonal crystals, indicates that the metal-to-ligand distance changes upon doping. The obtained set of parameters concerning one defect in various analogous environments can furthermore be used to test different methods of theoretical calculations for ZFS and SHF values.

Introduction

Fluoroelpasolite crystals with general formula $A^I_2B^IM^{III}F_6$ are very interesting hosts for trivalent Transition Metal (TM) and rare earth ions. They allow incorporation of such ions in sites of (nearly) octahedral symmetry without need for charge compensation. As a result, high doping concentrations can be attained, which are necessary in many optical applications, *e.g.* in crystals intended as active medium in solid state lasers. Another beneficial property of these fluoride crystals is their reduced phonon cut-off frequency in comparison with the more common oxide crystals, as a result of which the probability of non-radiative decay is reduced. The present study concerns Cr^{3+}-doped hexagonal Cs_2NaMF_6 (M = Al or Ga) crystals, which are considered as active media for tuneable lasers in the near IR,[1] and Er^{3+}-doped cubic Cs_2NaYF_6 crystals, which have been studied for their possibility to act as vacuum UV scintillators[2] and mid IR emitters.[3]

As has been determined by Electron Paramagnetic Resonance (EPR),[4,5] optical spectroscopy[1] and X-Ray Diffraction (XRD),[6,7] the hexagonal crystals have two distinct M^{3+} sites (Table 1) at which trivalent dopant ions can be incorporated, both with nearly octahedral symmetry. The two sites are illustrated in Fig. 1: one of them is slightly compressed (Fig. 1b) and the other slightly elongated (Fig. 1c) along the trigonal *c* axis of the crystal. In the cubic Cs_2NaYF_6 crystal,[8] all Y^{3+} positions are equivalent and have perfect octahedral symmetry (Fig. 1a).

Fe^{3+} has been found as common impurity in all these crystals,[5,6] like in many other optical materials, *e.g.* Nd:YAG,[9] CdTe[10] and CaB_6.[11] The precise effect of this impurity on the optical properties of such materials is not always fully understood or predictable. It is in any case important to be able to detect and identify the Fe^{3+} impurities, a task for which EPR and Electron Nuclear Double Resonance (ENDOR) are particularly well suited. As Fe^{3+} is an S-state ($^6S_{5/2}$ ground state) ion, its EPR spectrum can be recorded even at room temperature (*RT*).

Recently, considerable attention has been paid to calculations of optical transition energies, crystal field level splittings, *g* tensors and Zero Field Splitting (ZFS) parameters for TM ion centres in fluoride and oxide crystals, in order to evaluate doping-induced crystal distortions *via* spectroscopic properties and/or to predict spectroscopic properties of new host:dopant combinations. As *ab initio*, *e.g.* Density Functional Theory (DFT), methods for reliable calculation of ZFS parameters have only recently become available,[12] calculations based on second order perturbation expressions and/or superposition models are commonly used in such studies.[13] On the other hand, the theory for calculating hyperfine interaction parameters from first principles is well-developed, although calculations for systems with $S > \frac{1}{2}$ are still quite challenging and only rarely encountered in literature.[14] As will be shown, our

---

[a] *Department of Solid State Sciences, Krijgslaan 281 – S1, B-9000 Gent, Belgium. E-mail: freddy.callens@ugent.be; Fax: +32(0)92644996; Tel: +32(0)92644352*
[b] *Institute of General and Inorganic Chemistry, 31 Leninskii Prospect, 119991 Moscow, Russian Federation*
[c] *Physics Department, University of Antwerp, Universiteitsplein 1, B-2610 Antwerpen (Wilrijk), Belgium*

Table 1 Description of the surroundings of the M^{3+} ion in Cs_2NaMF_6, using the structural data of ref. 6–8. For each shell, the number of equivalent ions and their distance to the central M^{3+} ion is given. In the last column, the deviation from a perfect cube is given, with $\theta_{reg} = 54°44'$ and θ_{MF_6} the angle between a C_3 axis and a C_4 axis in a perfect octahedron, respectively between a C_3 axis and the M–F direction for the first shell F^- neighbors of the M^{3+} ion (Fig. 1c)

Shell	Ion	Number	Distance/Å	$\theta_{reg} - \theta_{MF_6}$
M^{3+} in a cubic site (Cs_2NaYF_6)				
0	M^{3+}	1	0	0
1	F^-	6	2.269	
2	Cs^+	8	3.93	
3	Na^+	6	4.538	
M^{3+} in the trigonally compressed site				
			Distance/Å Cs_2NaAlF_6/Cs_2NaGaF_6	$\theta_{reg} - \theta_{MF_6}$ Cs_2NaAlF_6/Cs_2NaGaF_6
0	M^{3+}	1	0	−16′/−27′
1	F^-	6	1.822/1.902	
2	Cs^+	6 + 2	3.9/3.9	
3	Na^+	6	4.118/4.167	
M^{3+} in the trigonally elongated site				
			Distance/Å Cs_2NaAlF_6/Cs_2NaGaF_6	$\theta_{reg} - \theta_{MF_6}$ Cs_2NaAlF_6/Cs_2NaGaF_6
0	M^{3+}	1	0	1°26′/1°32′
1	F^-	6	1.815/1.901	
2	Na^+	2	2.930/2.957	
3	Cs^+	6	3.775/3.790	

EPR and ENDOR study has enabled to accurately determine both the signs and the magnitudes of the ZFS and ^{19}F SuperHyperFine (SHF) parameters for several $(FeF_6)^{3-}$ complexes which are expected to reflect the properties of the crystal sites and thus to slightly differ in Fe^{3+}–F^- distance and degree of trigonal distortion. These data thus present a challenging test for theoretical calculations.

The Fe^{3+}-ion has an (Ar)3d^5 configuration. In an octahedral crystal field Fe^{3+} has electronic spin $S = 5/2$ and a g factor close to 2 ($L = 0$). Even in perfect cubic symmetry, such systems exhibit a small ZFS which has to be included in the total spin Hamiltonian (SH):

$$\hat{\mathrm{H}} = \beta_e \overrightarrow{B}\cdot\overleftrightarrow{g}\cdot\hat{\vec{S}} + \hat{H}_{ZFS} + \sum_i \left(\hat{\vec{S}}\cdot\overleftrightarrow{A}_i\cdot\hat{\vec{I}}_i - \beta_N g_{N,i}\vec{B}\cdot\hat{\vec{I}}_i + \hat{\vec{I}}_i\cdot\overleftrightarrow{Q}\cdot\hat{\vec{I}}_i\right) \qquad (1)$$

The first term on the right hand side of eqn (1) represents the electronic Zeeman energy, parameterised by the g tensor, the second is the ZFS term. The terms between brackets represent interactions with neighbouring nuclei. These include hyperfine interactions of the electron spin S with the six ^{19}F nuclei ($I = 1/2$, $g_N = 5.258$) and with more remote ^{23}Na nuclei ($I = 3/2$, $g_N = 1.478$), and corresponding nuclear Zeeman interaction terms. For ^{23}Na nuclei, a nuclear quadrupole interaction (last term in eqn (1)) also has to be taken into account.

The ZFS term in the SH deserves some further attention. For $S = 5/2$ in a trigonally distorted octahedral site, it becomes

$$\hat{H}_{ZFS} = B_2^0\hat{O}_2^0 + B_4^0\hat{O}_4^0 + B_4^3\hat{O}_4^3. \qquad (2)$$

where $\hat{O}_k^q = \hat{O}_k^q\ (\hat{S}_x, \hat{S}_y, \hat{S}_z)$ represent the extended Stevens operators.[15,16]

In cubic symmetry, as expected for Fe^{3+} substituting Y^{3+} in the cubic Cs_2NaYF_6 elpasolite crystals, $B_2^0 = 0$ and the fourth rank ZFS parameters are related by

$$B_4^3 = 20\sqrt{2}B_4^0, \qquad (3)$$

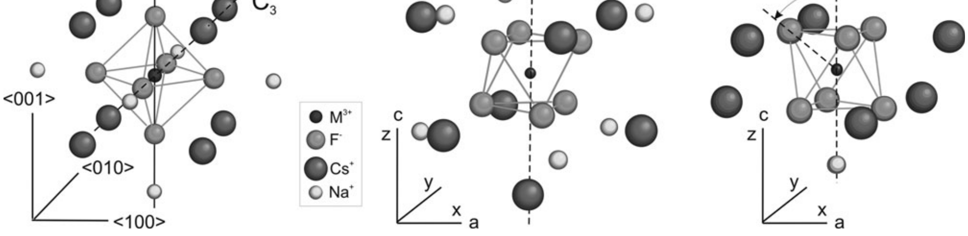

Fig. 1 Lattice surroundings of the M^{3+} ions in a cubic elpasolite (a) in the regular octahedral site R and in a hexagonal elpasolite: (b) in the trigonally compressed site C and (c) in the trigonally elongated site E. The M^{3+}–F^- distances and declination angles with respect to the C_3 ⟨111⟩ symmetry axis of the complexes, θ_{MF_6} (see (c)) for the various sites in the three crystals, are listed in Table 1.

taking a C_3 axis of the centre as z-axis. In the case of cubic symmetry, it is more common to analyse the spectra in a tetragonal crystal frame taking the z-axis along a C_4 axis (Fig. 1a). For comparison with literature data of Fe^{3+} centres in other cubic sites, we note that[17,18]

$$\hat{H}^{\text{cubic}}_{\text{ZFS}} = [B_4^0]_{\text{tetra}}(\hat{O}_4^0 + 5\hat{O}_4^4) \text{ with } [B_4^0]_{\text{tetra}} = -\frac{3}{2}B_4^0. \quad (4)$$

Our EPR and ENDOR analysis allowed to determine both values and signs of all the interaction parameters discussed above.

Experimental

The fluoroelpasolite crystals were synthesized under hydrothermal conditions.[1,2] Cs_2NaYF_6 was doped with Er^{3+}, the two hexagonal crystals (Cs_2NaMF_6, M = Ga or Al) had Cr^{3+} as intentional dopant, with concentrations of approximately 0.1 at%. All elpasolites contained Fe^{3+} as impurities in an unknown concentration.

EPR and ENDOR spectra were recorded at X band (9.5 GHz) on a Bruker ESP300E spectrometer with a ESP353 ENDOR-Triple extension and at Q band (34 GHz) on a Bruker ElexSys E500 spectrometer. Both spectrometers are equipped with an Oxford flow cryostat, respectively an ESR910 (2–300 K) and a CF935 (4.2–300 K).

The W band EPR experiments were performed using a continuous wave W band EPR spectrometer (Bruker ElexSys E680) with a cylindrical cavity operating at 94 GHz and a split coil superconducting magnet (Oxford). The system was equipped with a continuous flow helium cryostat (4.2–300 K).

The spectra were analysed using the EasySpin[16] routines.

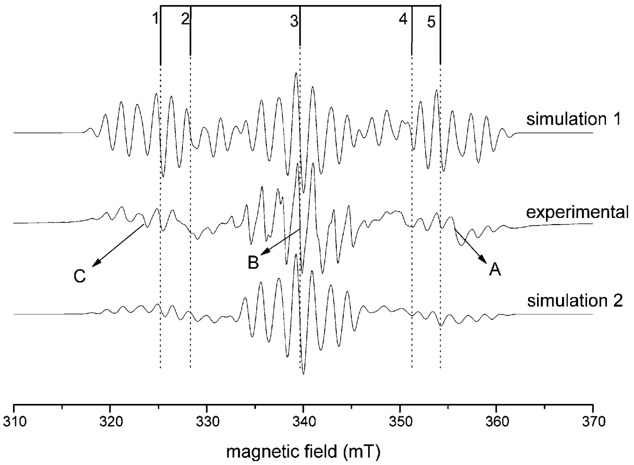

Fig. 2 EPR spectrum of Cs_2NaYF_6:Fe^{3+}, with $B \parallel \langle 100 \rangle$ at X band (ν = 9.513 GHz, T = 8 K). The middle spectrum represents the experimental spectrum. The upper spectrum (simulation 1) shows a simulation without strain in the B_4^0 parameter, the lower spectrum (simulation 2) with a Gaussian distribution (full width at half maximum 0.37 MHz) in the B_4^0 parameter. At the top, the five lines due to the ZFS are indicated. The spectra were recorded with P_{mw} = 1 mW and a modulation amplitude of 0.1 mT. A, B and C indicate the positions for the ENDOR spectra of Fig. 4.

Fe^{3+} in the cubic elpasolite Cs_2NaYF_6

EPR analysis. The X band EPR spectrum at 8 K near $g \approx 2$ of Cs_2NaYF_6 in the $\langle 100 \rangle$ direction is shown in Fig. 2 (middle line). For an Fe^{3+} impurity with cubic symmetry, five allowed unsplit EPR lines are expected, since the magnetic isotope ^{57}Fe ($I = \frac{1}{2}$) has only 2% of natural abundance. This five lines structure cannot easily be recognised in the multiline EPR spectrum, due to an additional splitting as a result of the SHF interaction with the six ^{19}F nuclei in the first shell. As the EPR spectrum is quite complex, the SHF tensor for this interaction can be more easily deduced from the ENDOR spectrum. The complete ENDOR analysis will be discussed below and the obtained SHF parameters are listed in Table 2. Using these, we were able to unravel the EPR spectrum and to extract the B_4^0 ZFS parameter, also listed in Table 2. The simulated EPR spectrum using these SHF and ZFS parameters (simulation 1 in Fig. 2), however, shows a remarkable difference in the intensities of the outer SHF packets, as compared to the experimental spectrum. This discrepancy is removed to a large extent by allowing for a (Gaussian) distribution in the B_4^0 parameter retaining cubic symmetry (eqn (3)), which may reflect random strain in the crystal. The linewidth of the central SHF packet, the position of which is only affected to second order by B_4^0, is indeed smaller than for the outer multiplets, which bear first order ZFS contributions. In simulation 2 in Fig. 2, a Gaussian distribution in B_4^0 (and thus also in B_4^3) is assumed, with a full width at half maximum of 0.37 MHz. This simulation agrees much better with experiment, regarding line intensities. The sign of B_4^0 could only be determined relative to that of the ^{19}F hyperfine parameters, as explained below.

The remaining differences between the experimental and simulated spectrum may be attributed to the composite nature of the spectrum, as illustrated in the W band spectrum in Fig. 3. In the spectra contributions of three impurities are distinguished. First, centred around B_0 = 3353 mT (g_{eff} = 2.003) we observe the Fe^{3+} spectrum with its fine and SHF structure, the subject of this study. Second, at B_0 = 3372 mT (g_{eff} = 1.992) seven accidentally coincident lines of a Gd^{3+} ($^8S_{7/2}$ ground state) impurity occur. And third, at B_0 = 3403 mT (g_{eff} = 1.958) the SHF split resonance line of a Cr^{3+} impurity is found. The latter two impurities have earlier been identified in Cs_2NaYF_6 and the ZFS and SHF parameters used in the simulation in Fig. 3 are taken from ref. 19.

ENDOR analysis. In the ENDOR spectrum, interactions with the first coordination shell of the Fe^{3+} ion, consisting of 6 equivalent ^{19}F nuclei, are observed. The cubic symmetry of the centre requires that their A tensors are axially symmetric around the metal–ligand axis. For $\vec{B} \parallel \langle 100 \rangle$, two nuclei along the $\langle 100 \rangle$ axis thus exhibit an interaction constant $A_\parallel$ and four nuclei in the 100 plane have an interaction strength $A_\perp$. If the $M_s \rightarrow M_s + 1$ EPR transition is saturated, the following two ENDOR transitions are to first order expected for each of these sets of nuclei

$$\begin{cases} h\nu_{\text{ENDOR}} = |AM_S - g_N\beta_N B| \\ h\nu_{\text{ENDOR}} = |A(M_S + 1) - g_N\beta_N B| \end{cases}. \quad (5)$$

Table 2 Spin Hamiltonian parameters (errors in the last digits given as subscripts) for all discussed crystals, as extracted from the analysis of the angular variation of the EPR and ENDOR spectra. All parameters are expressed in the reference frame of the concerned site for reasons of comparison; this is especially important for B_4^3 (see text). θ_A is the angle between a C_3 axis and the principle $A(^{19}F)$ direction

	$Cs_2NaYF_6:Fe^{3+}$	$Cs_2NaAlF_6:Fe^{3+}$		$Cs_2NaGaF_6:Fe^{3+}$	
Site	R	C	E	C	E
g	2.0028_{20}	2.0023_{11}	2.0022_{18}	2.0023_{10}	2.0023_{12}
B_2^0/MHz	—	$215.5_{3.4}$	$-244.7_{3.7}$	$180.0_{2.6}$	$-216.3_{2.8}$
B_4^0/MHz	-0.90_3	-0.98_{13}	-1.24_{16}	-0.95_{11}	-1.19_{14}
B_4^3/MHz	-25.36_{85} [a]	$-27.4_{4.0}$	$-36.4_{9.5}$	$-28.3_{4.1}$	$-37.2_{6.7}$
A_x (^{19}F)/MHz	44.5_6	47.48_{80}	43.65_{80}	47.33_{60}	43.82_{72}
A_y (^{19}F)/MHz	44.5_6	47.64_{99}	$45.3_{1.1}$	47.08_{99}	44.57_{89}
A_z (^{19}F)/MHz	$103.7_{1.0}$	106.70_{78}	106.60_{74}	106.16_{59}	106.08_{70}
θ_A (^{19}F)	$54°44'$	$55°15'_{27'}$	$52°45'_{29'}$	$55°17'_{26'}$	$53°0'_{29'}$
$A_\perp$ (^{23}Na)/MHz			-0.87_4		-0.90_4
$A_\parallel$ (^{23}Na)/MHz			1.34_4		1.32_4
$\lvert Q_\perp \rvert = \lvert Q_\parallel/2 \rvert$ (^{23}Na)/MHz			0.034_{10}		0.022_{10}

[a] For the cubic case we assumed that $B_4^3 = 20\sqrt{2}B_4^0$.

$A_\parallel$ and $A_\perp$ were determined by fitting resonance positions in the X band ENDOR spectra with $\vec{B} \parallel \langle 100 \rangle$ at different field positions and the obtained parameters are listed in Table 2, where $A_x = A_y = A_\perp$ and $A_z = A_\parallel$. An ENDOR angular variation at Q band confirmed these values. In principle, their absolute signs cannot be determined from the ENDOR spectra. However, in $KMgF_3:Fe^{3+}$ it was unambiguously shown[20] that $A_{\perp,\parallel}(^{19}F) > 0$ and theoretical calculations[21] also predict that the sixfold coordinated iron impurity in fluorides has a large positive isotropic SHF parameter. Hence, we assume here that $A_{\perp,\parallel}(^{19}F) > 0$.

Fig. 4 shows three X band ENDOR spectra at different field positions (marked in Fig. 2). Because different $M_s \rightarrow M_s + 1$ transitions are saturated at the different field positions, a large difference between the spectra is observed, as predicted by eqn (5). This allows to determine the sign of B_4^0 relative to $A_\parallel$ and $A_\perp$ as follows. In zero magnetic field, the $2S + 1$ levels split into a quartet and a doublet, separated by $540|B_4^0|$. The doublet has the lowest energy for $B_4^0 < 0$, if $B_4^0 > 0$ the quartet lies lowest, as illustrated in the energy level schemes of Fig. 5. In case of a negative B_4^0, the high field part of the EPR spectrum (position A in Fig. 2, transition 5 in Fig. 5) corresponds to the $1/2 \rightarrow 3/2$ transition and the low field part (position C, transition 1 in Fig. 5) to $-3/2 \rightarrow -1/2$, and the other way around for positive B_4^0. Some problems occurred during analysis: (i) not all the lines which appeared in the ENDOR spectra could be explained, (ii) not all expected lines were present and (iii) due to overlapping SHF packets, other EPR transitions were also saturated (*e.g.* $5/2 \leftrightarrow 3/2$ at position C). Q band ENDOR was thus needed to supply a more convincing picture (see below, Fig. 5).

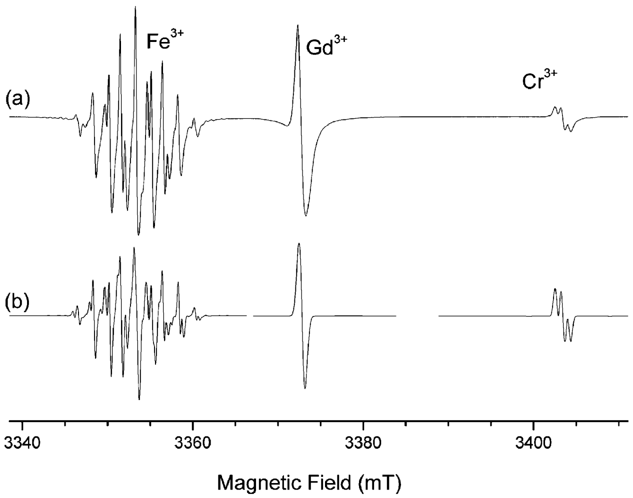

Fig. 3 Experimental (a) and simulated (b) W band EPR spectrum of $Cs_2NaYF_6:Fe^{3+}$, Gd^{3+}, Cr^{3+} at 94.01 GHz (polar angles of the magnetic field in relation to the $\langle 100 \rangle$ axis: $\theta = 30°$ and $\phi = 45°$). $T = 20$ K, $P_{mw} = 0.44$ μW, $A_{mod} = 0.1$ mT.

Some transitions in the ENDOR spectra in Fig. 4 exhibit an additional splitting, which disappears in the Q band spectrum and is thus due to second order interactions between equivalent nuclei *via* the electron spins.[22] These features are very well reproduced in simulations, an example of which is shown in the inset in Fig. 4.

At Q band a complete field variation of the ENDOR spectrum was recorded for B approximately along $\langle 100 \rangle$. This is represented in the two dimensional EPR-ENDOR plot in Fig. 6. It confirms our sign assignation of B_4^0 and gives a clear overview of which M_S states are involved in the saturated EPR transitions at each magnetic field position. For example, ENDOR transitions within the $M_S = 5/2$ state are most efficiently excited in the low field wing of the EPR spectrum, which can only be explained when $B_4^0 < 0$. The variation of the ENDOR line positions as a function of the magnetic field strength can easily be explained from eqn (5), which for positive ^{19}F principal hyperfine values predicts that the ENDOR frequency within negative (positive) M_S states goes up (down) with increasing magnetic field.

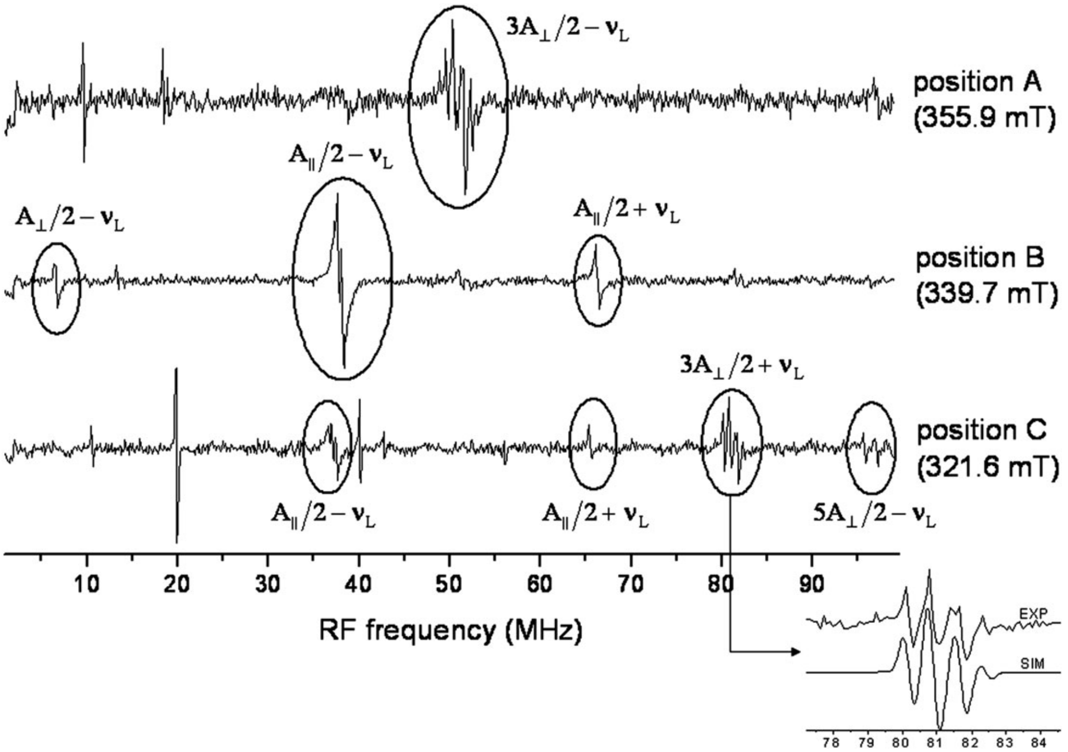

Fig. 4 X band ENDOR of Cs$_2$NaYF$_6$:Fe^{3+} with $\vec{B} \parallel \langle 100\rangle$, at the magnetic field positions indicated in Fig. 2. The encircled line packets are attributed to the SHF interaction with the six equivalent ^{19}F nuclei in the first coordination shell. For this magnetic field orientation, the two ^{19}F nuclei along the $\langle 100\rangle$ axis exhibit a SHF interaction with strength $A_\parallel$ while for the other four it is $A_\perp$. The transitions are labelled with the first order expression of their ENDOR frequency, in which $\nu_L = g_N\beta_N B$ represents the ^{19}F Larmor Frequency, from which the M_S multiplet can be determined through eqn (5). The spectra were recorded at 6 K and with $\nu = 9.522$ GHz. The inset shows a detail of the additional splitting observed in certain ENDOR lines, due to interactions between the equivalent nuclei *via* the electron spin, along with a simulation.

Fe^{3+} in hexagonal fluoroelpasolites

For both crystals EPR spectra were recorded at Q band and the $\vec{B} \parallel c$ spectrum of Cs$_2$NaGaF$_6$ is shown in Fig. 7a. For $\vec{B} \parallel c$, all six surrounding ^{19}F nuclei are equivalent, giving rise to well separated SHF patterns (with 1 : 6 : 15 : 20 : 15 : 6 : 1 intensity ratios), since the ZFS is larger than in the cubic crystals due to the axial distortion of the octahedra along the c

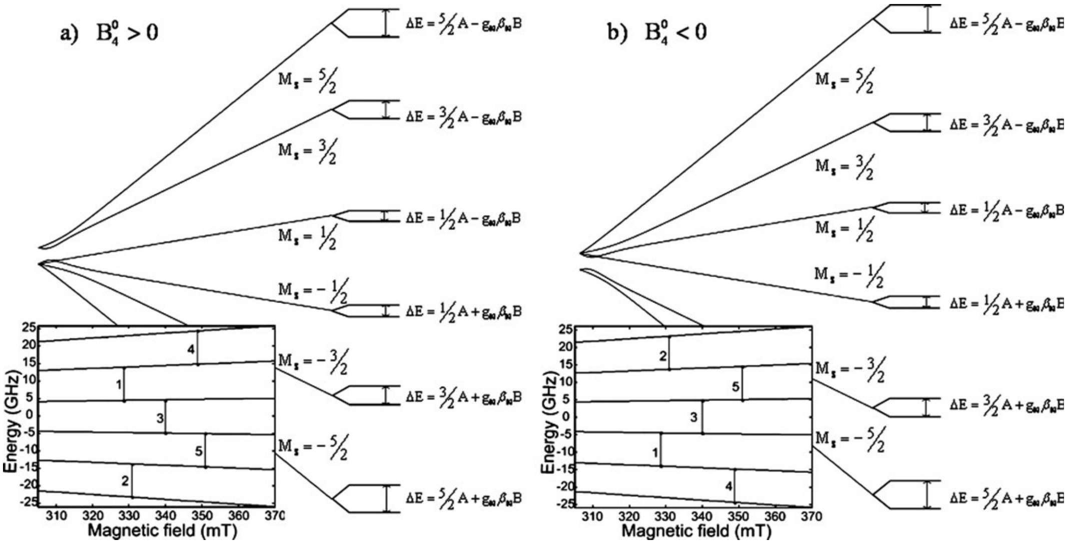

Fig. 5 Energy level scheme for an $S = 5/2$ ion in a cubic crystal field ($B_4^3 = 20\sqrt{2}B_4^0$) with $B_4^0 > 0$ (a) or $B_4^0 < 0$ (b), interacting with one $I = 1/2$ nucleus, with an external magnetic field $\vec{B} \parallel \langle 100\rangle$. The superhyperfine splittings are exaggerated, for clarity reasons, and it is assumed that A, $g_N > 0$. The insets give the calculated energy level scheme without an interacting $I = 1/2$ nucleus. The vertical lines indicate resonance field positions for $\nu = 9.51$ GHz and $|B_4^0| = 0.90$ MHz.

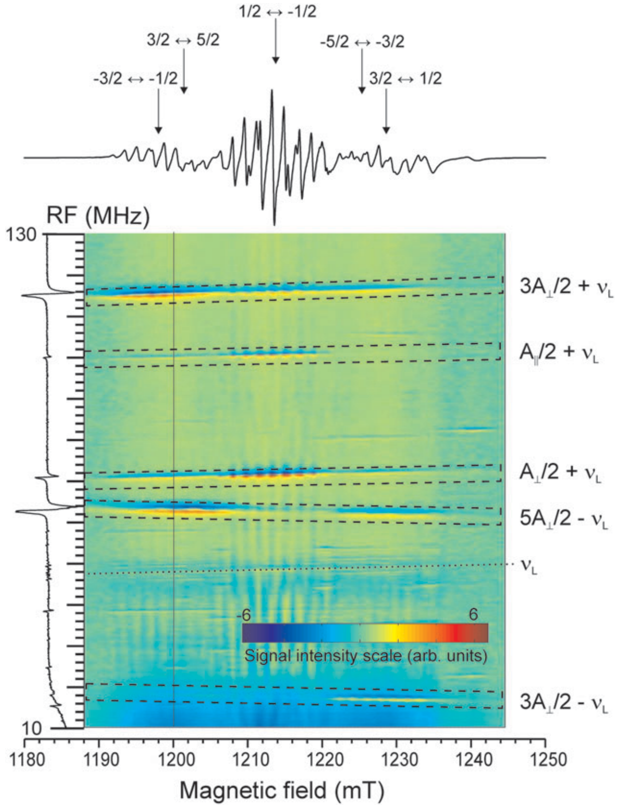

Fig. 6 Two dimensional intensity (square root of intensity for contrast enhancement) plot of first derivative ENDOR spectra as a function of magnetic field for Cs_2NaYF_6:Fe^{3+} at $\nu = 34.010$ GHz and $T = 12$ K. The EPR spectrum is shown on the top and the ENDOR spectrum at $B = 1200$ mT (indicated with full line in the 2D plot) is shown on the left The spectra were recorded with $P_{\mathrm{mw}} = 2$ mW and $P_{\mathrm{RF}} = 200$ W. The transitions are labelled with the first order expression of their ENDOR frequency (eqn (5)), and the position of the ^{19}F Larmor frequency ν_{L} corresponding to interactions with distant nuclei, is marked as well.

axis. As there are two inequivalent Fe^{3+} sites (Fig. 1), ten zero field split SHF packets are expected. Only eight are visible, though, since the $-\frac{1}{2} \rightarrow \frac{1}{2}$ transition for both sites overlap and one SHF packet is hidden under the more intense Cr^{3+} lines. The two EPR spectra can be well separated and linked to sites E and C, on the basis of their ^{23}Na ENDOR spectrum presented in Fig. 7b.

^{23}Na ENDOR analysis. The analysis of the ^{23}Na ENDOR spectra is essentially analogous to that for the Cr^{3+} centres[4] in these crystals. For site E (Fig. 1c), the closest ^{23}Na shell ($r < 3$ Å) consists of two equivalent nuclei along the c-axis, resulting, when $\vec{B} \parallel c$, in two widely split triplets (separated by $A_{\parallel}$) in the ^{23}Na ENDOR spectrum. This is illustrated for Cs_2NaGaF_6 in the ENDOR spectrum at $B = 1112.8$ mT in Fig. 7b. Six equivalent ^{23}Na nuclei ($r > 4.1$ Å) on off-axis positions with a smaller HF interaction characterise site C (Fig. 1b). The corresponding ENDOR spectra are broader and show a narrower splitting (*e.g.* ENDOR spectrum at $B = 1145.1$ mT in Fig. 7b). Based on these qualitative differences between the ENDOR spectra, we could assign each EPR transition to a particular site and at $B = 1212.9$ mT the spectra of both sites clearly overlap. The spectra with $\vec{B} \perp c$ were decomposed in an analogous way.

After analysis (results shown in Table 2), we find for the ^{23}Na SHF interaction of the E site that $A_{\parallel} > 0$ and $A_{\perp} < 0$. The relative sign of Q(^{23}Na) could not be determined, as the corresponding SHF interaction is not resolved in the EPR spectrum.[4] A complete analysis of the ^{23}Na interaction of site C has not been attempted. Analogous results were obtained for Cs_2NaAlF_6 and the results can also be found in Table 2.

EPR analysis. In Fig. 8a the EPR angular variation for the Cs_2NaAlF_6 crystal in a plane containing the c axis is shown, with simulations for the central EPR lines of the SHF packets. Since the SHF packets overlap when the magnetic field is rotated away from the c axis, the five ZFS components cannot be separated well enough to allow an accurate determination the B_4^3 parameter, and within experimental error we found the B_4^0 and B_4^3 parameters to be related by eqn (4) like for the site R.

As for the signs of the B_4^3 parameters, one should note an important difference between the E and the C sites, not commented upon until now. Inspecting Fig. 1, where the three $(MF_6)^{3-}$ sites are presented in the same crystal axis system, one can see that the C octahedron is obtained from the R octahedron by a rotation over $\alpha = 45°$ around the C_4 axis, followed by a rotation over $\beta = 54°44'$ around the new y axis, whereas for the E site $\beta = -54°44'$. This results in a $\phi = 60°$ shift around the c axis between the octahedra of site C and site E, or between their reference frames in a common axis system (*e.g.* a single crystal). When analysing the EPR and coupled ENDOR spectra of the two sites in a common (crystal) axis system, the B_4^3 parameter and the θ_{A} angle, defining the principal z orientation of the ^{19}F A tensors, have opposite signs for the two centres. The relation between the B_4^3 parameters can be deduced from the transformation properties for $\hat{O}_k^q$ parameters in ref. 18. The parameters of each site in Cs_2NaAlF_6 are shown in Table 2, as well as the parameters for Cs_2NaGaF_6 which were obtained in the same way. The parameters were used for the simulation in Fig. 8a.

From 20 K Q band measurements, again only the relative signs of the B_k^q parameters of each site could be obtained. At W band, though, the microwave quantum is large enough to observe thermal population effects at low temperatures. Indeed, as the electronic Zeeman energy clearly dominates the SH at resonance conditions (Fig. 5), the states with high M_{S} become depopulated at low temperatures, which allows to determine the absolute sign of the ZFS parameters. In Fig. 9 these effects are shown for Cs_2NaAlF_6 with $\vec{B}$ approximately parallel to c. At the bottom (Fig. 9c), EPR spectra at different temperatures are shown, while at the top two possible sign assignations are drawn. Fig. 9a shows the situations when $B_2^0 > 0$ for site C and $B_2^0 < 0$ for site E, in Fig. 9b the reverse situation is drawn. The signs for the other B_k^q parameters follow from the sign of B_2^0. While lowering the temperature, it becomes obvious from Fig. 9c that the situation of Fig. 9a is correct. Indeed, for site E (site C), *e.g.*, transitions 7 and 10 (2 and 3) become more intense in comparison with transition 1 (9) when the temperature rises.

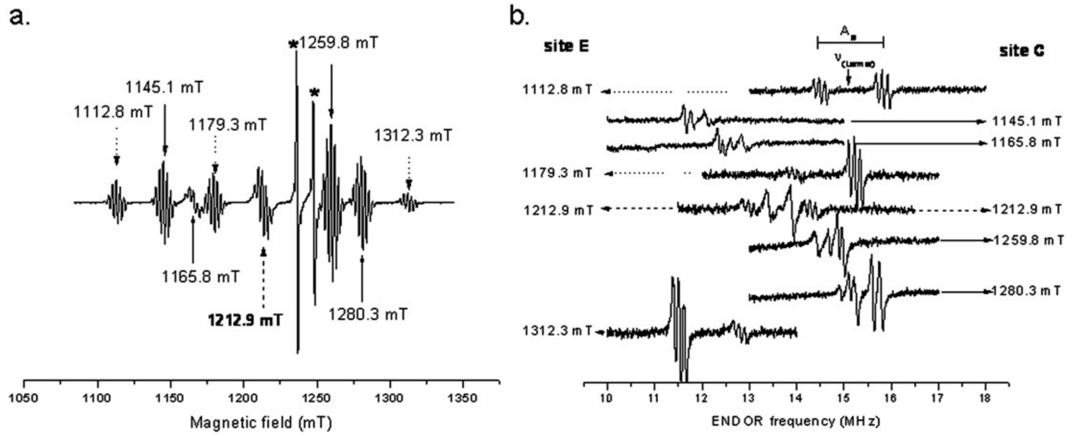

Fig. 7 (a) Q band EPR spectrum of Cs_2NaGaF_6:Fe^{3+} with $\vec{B} \parallel c$ at $T = 20$ K. The 2 intense lines (marked with asterisks) belong to the Cr^{3+}-ion. (b) ^{23}Na ENDOR spectra of site C and site E, recorded at various field positions at $T = 10$ K (indicated on the left: solid arrows for site C, dashed arrows for site E). At 1212.9 mT the lines for the sites coincide and the typical ^{23}Na ENDOR spectrum of both sites is present.

^{19}F ENDOR analysis. The ENDOR angular variation of the ^{19}F interactions, measured at the $-\frac{1}{2} \rightarrow \frac{1}{2}$ EPR transition is shown in Fig. 8b. For an arbitrary magnetic field orientation, the ENDOR spectrum is the result of an interaction with three magnetically inequivalent sets of two ^{19}F nuclei. The SHF tensors of these sets are transformed into one another by rotations over 120° around the *c*-axis. They are determined by only four free parameters (A_x, A_y, A_z, θ_A = declination from the *c* -axis) as symmetry requires that one principal direction (A_y) is perpendicular to the plane containing the *c* axis and the Fe^{3+}–F^- bond direction. The simulation with the best-fit values for the two sites (Table 2) is also shown in Fig. 8b and perfectly reproduces the experimental angular pattern. If $\vec{B} \parallel c$, for each site, the ENDOR spectra of the six fluorine nuclei are expected to coincide, but due to a slight misorientation of the crystal, this is not exactly the case in the experimental angular variation. The analysis of the ENDOR spectra and the observed SHF structure in the EPR spectra allow us to conclude that all six ^{19}F nuclei in the first shell are equivalent. The symmetry of the FeF_6 complexes is thus indeed D_{3d}. This rules out the possibility that the deviation from cubic symmetry of the centres is caused by an off-centre displacement of the Fe^{3+} ion along the *c* axis, rather than by a simple symmetric compression or elongation of the coordination octahedron along the *c* axis. This could not be excluded from analysis of the *g* tensor and ZFS parameters alone.

As in the cubic case, the relative signs of the SHF and ZFS parameters were determined by recording ENDOR spectra at different $M_S \rightarrow M_S + 1$ EPR transitions. For Cs_2NaAlF_6 we could use the unambiguously determined signs of the B_k^q parameters and found that $A_i(^{19}F) > 0$ ($i = x, y, z$). This gives the assumption that $A_{\parallel,\perp}(^{19}F) > 0$ in Cs_2NaYF_6 further support. Assuming $A_i(^{19}F) > 0$ for Cs_2NaGaF_6, we find $B_2^0 > 0$ for site E and $B_2^0 < 0$ for site C, in perfect analogy with Cs_2NaAlF_6.

Discussion and conclusions

Some general qualitative conclusions can be made about the SH which a reliable theoretical modelling of these complexes should at least be able to reproduce.

From the ^{19}F ENDOR data, it was found that the principal direction of the ^{19}F SHF tensors correlates with the Al^{3+}/Ga^{3+}/Y^{3+}–F^- direction: θ_A (Table 3) corresponds very well with θ_{MF_6} (Fig. 1 and Table 1). In the case of a pure point dipole interaction between electron and nuclear spin, one can calculate that the anisotropic part of the superhyperfine tensor is axially symmetric around the Fe^{3+}–F^- axis (*z*-axis):[22]

$$A = A_{\mathrm{dip}} \begin{pmatrix} -1 & 0 & 0 \\ 0 & -1 & 0 \\ 0 & 0 & 2 \end{pmatrix} \text{ with} \\ A_{\mathrm{dip}} = \frac{\mu_0}{4\pi} \frac{g \cdot g_N \cdot \beta_e \cdot \beta_N}{R^3}, \tag{6}$$

and β_e and β_N representing the Bohr and nuclear magneton, respectively. In Table 3, the values of A_{dip} for the various centres, calculated with the original R = M^{3+}–F^- distance (M^{3+}:Al^{3+}, Ga^{3+} or Y^{3+}), are shown. These can be compared with the anisotropic part of the measured SHF tensors, defined as

$$A_{\mathrm{aniso}} = \frac{1}{3} \cdot \left(A_z - \frac{A_x + A_y}{2} \right). \tag{7}$$

First of all we note that, for all ^{19}F interactions, the measured A_{aniso} is considerably larger than A_{dip}, which points to a significant overlap or covalency contribution to the SHF interaction. In addition, it is clearly seen that these two properties do not exhibit the same variability. A_{aniso} seems to be almost independent of the M^{3+}–F^- distance in the crystal, which suggests that the M^{3+}–F^- distance, in accordance with theoretical findings,[20] changes upon doping.

On the other hand, for the ^{23}Na interaction of the E site, the calculated A_{dip} is in good agreement with A_{aniso} (Table 3), suggesting that the M^{3+}–Na^+ distance does not change much upon doping. Note that all distances in Table 1 are determined from RT XRD measurements,[7] while the SHF interactions correspond to the situation at $T \approx 10$ K.

The ZFS parameters listed in Table 2, for which both signs and magnitudes could be accurately determined, also provide structural information on the Fe^{3+} sites. At first, we have

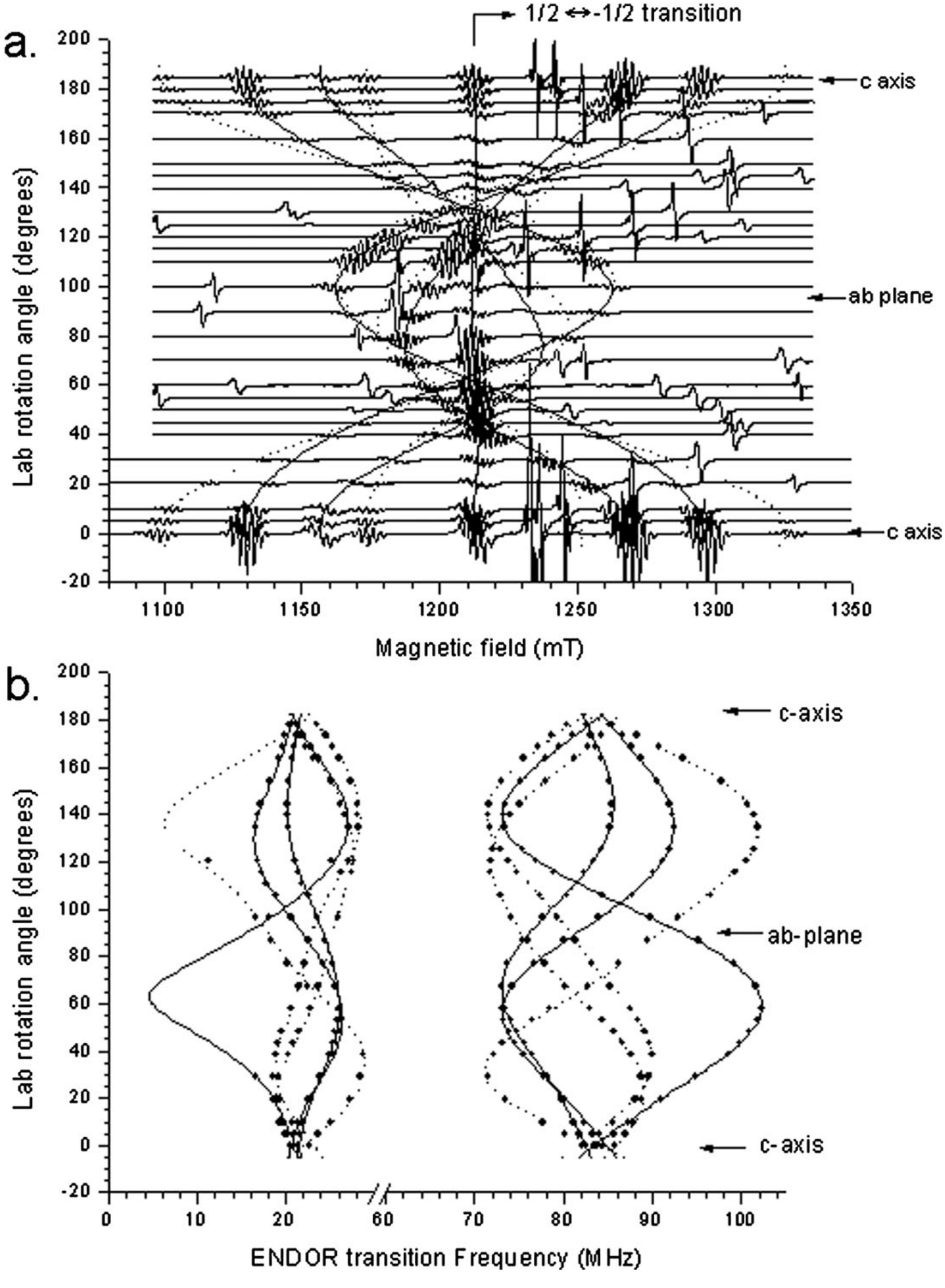

Fig. 8 (a) Q band EPR angular variation of Cs_2NaAlF_6:Fe^{3+} at 10 K and ν = 33.97 GHz. The additional resonances which show no SHF splitting, belong to Cr^{3+} centres. (b) ENDOR angular variation of the first shell ^{19}F interactions in Cs_2NaAlF_6:Fe^{3+}. It was recorded at the $\frac{1}{2} \rightarrow -\frac{1}{2}$ EPR transition indicated in (a). The dashed (solid) lines in both (a) and (b), represent the simulation of site E (site C).

determined the signs of the ZFS parameters of the three crystals assuming that all ^{19}F hyperfine parameters were positive. Afterwards, the B_k^q of Cs_2NaAlF_6 were determined explicitly *via* W band EPR measurements at variable (low) temperatures, and the signs correspond perfectly with those acquired with the aforementioned supposition. This assures that the sign attributions are correct. Moreover, for all sites we found that B_4^0 is negative in the trigonal reference frame, or following eqn (5), positive in the tetragonal description. As already explained in the previous section, for the axial sites E and C, deviations from cubic symmetry could not be detected in the B_4^q parameters. The B_2^0 parameter, on the other hand, appears to be a very clear marker for the distortion of the site. The sign of B_2^0 seems to depend on the type of distortion: for

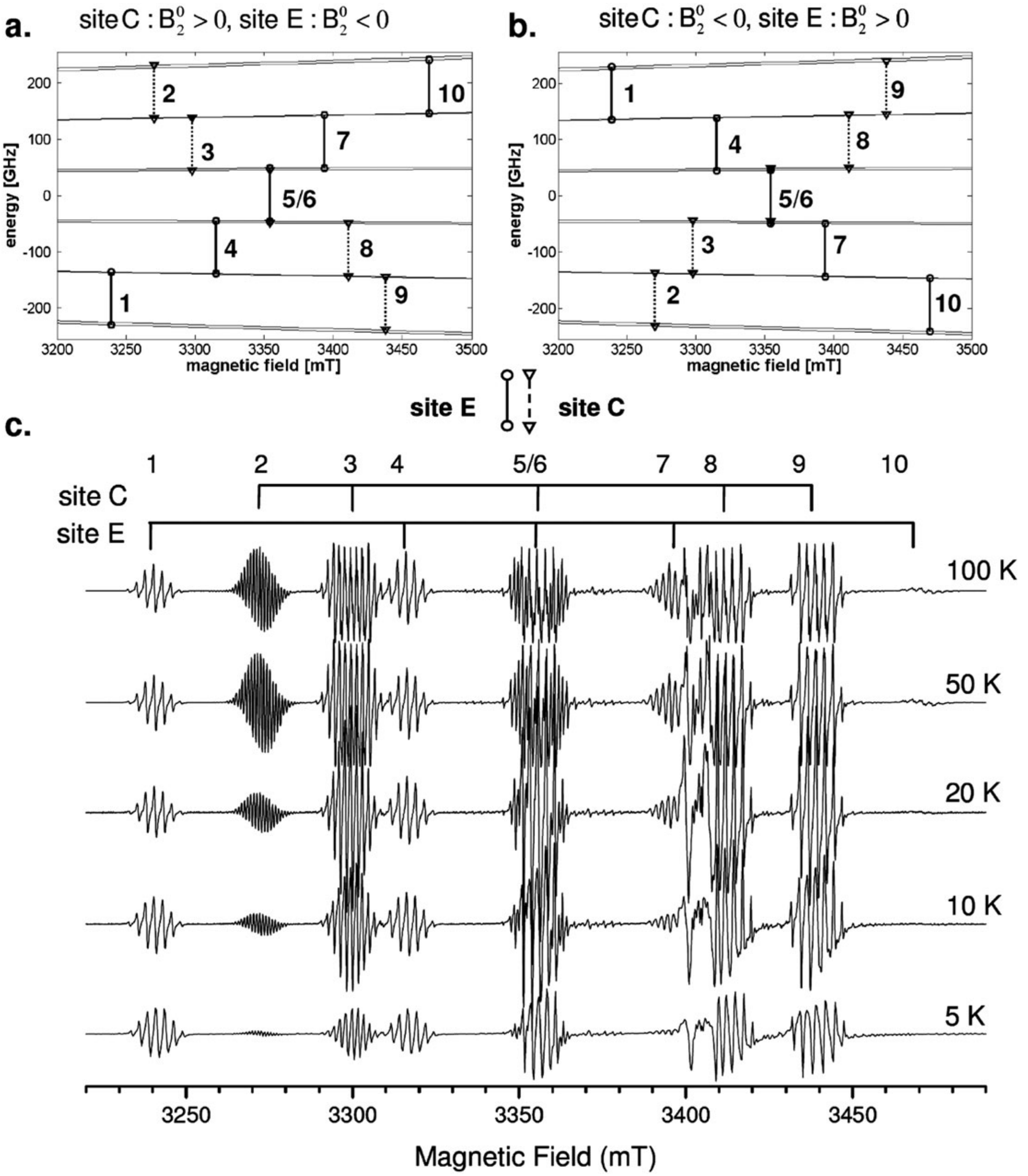

Fig. 9 W band EPR spectrum of Cs$_2$NaAlF$_6$:Fe^{3+} with ν = 94.067 GHz and $\vec{B} \parallel c$. At the top the energy levels are plotted with different sign choices for B_2^0 and with the circle ended full lines marking the transition fields for site E and the triangle ended dashed lines those for site C. (a) Shows the situation when $B_2^0 > 0$ for site C and $B_2^0 < 0$ for site E, (b) uses opposite signs for B_2^0. The B_k^q values are given in Table 2. (c) The EPR spectra at different temperatures are shown. The intense line around 3400 mT could be attributed to Cr^{3+}. The spectra have been normalized with respect to the low field signal around 3240 mT.

the elongated E site $B_2^0 < 0$ and the compressed C site $B_4^0 > 0$. Moreover, the magnitudes of B_2^0 are larger in site E than in site C and larger in Cs$_2$NaAlF$_6$ than in Cs$_2$NaGaF$_6$. The latter is to be expected, since the ionic radius of Fe^{3+} in a sixfold coordination (r = 69 pm) matches better with the radius of Ga^{3+} (r = 62 pm) than with Al^{3+} (r = 53 pm). This effect is also reflected in the larger ^{23}Na nuclear quadrupole interaction of site E in Cs$_2$NaAlF$_6$ as compared to Cs$_2$NaGaF$_6$.

Although the electronic ground states for Fe^{3+} (^{6}S) and Cr^{3+} (^{4}F) are different and great care should be taken when comparing the corresponding SH parameters, some characteristics of the E and C sites seem to be essentially independent of the impurity ion. The directions of the A tensor principal axes in both sites are comparable for the Fe^{3+} and the Cr^{3+} case. The same holds true for the ^{23}Na SHF interaction, probably reflecting the fact that this tensor can be mainly interpreted in a point dipole approximation, implying similar M^{3+}–Na$^+$ distances for Fe^{3+} and Cr^{3+} substitutions. A computational study will be necessary to explain all the subtleties of the observed effects, *e.g.* the systematic sign difference of the B_2^0 and A_{iso}(^{19}F) parameters between the two ions.

Table 3 Calculated values of hyperfine parameters from the ^{19}F and the ^{23}Na interactions with Fe^{3+}, using eqn (6) and (7)

Site	$Cs_2NaYF_6:Fe^{3+}$ Regular	$Cs_2NaAlF_6:Fe^{3+}$ Compressed	$Cs_2NaAlF_6:Fe^{3+}$ Elongated	$Cs_2NaGaF_6:Fe^{3+}$ Compressed	$Cs_2NaGaF_6:Fe^{3+}$ Elongated
^{19}F interaction					
$\theta_{reg}-\theta_A$ (^{19}F)	$0'$	$-31'$	$1°59'$	$-33'$	$1°44'$
$A_{dip}(^{19}F)$/MHz	6.36	12.33	12.54	10.84	10.84
$A_{aniso}(^{19}F)$/MHz	19.73	19.71	20.71	19.65	20.63
$A_{iso}(^{19}F)$/MHz	64.23	67.27	65.18	66.86	64.82
^{23}Na interaction					
$A_{dip}(^{23}Na)$/MHz	0.22	0.30	0.83	0.29	0.81
$A_{aniso}(^{23}Na)$/MHz			0.737		0.740

Acknowledgements

The authors, in particular H.V. and H.D.C., would like to thank the Flemish Research Foundation (FWO-Vlaanderen) for financial support. This research was partially supported by the FWO project G.0116.06.

References

1 (*a*) R. J. M. da Fonseca, A. D. Tavares, P. S. Silva, T. Abritta and N. M. Khaidukov, *Sol. Stat. Comm.*, 1999, **110**, 519–524; (*b*) L. P. Sosman, A. D. Tavares, R. J. M. da Fonseca, T. Abritta and N. M. Khaidukov, *Solid State Commun.*, 2000, **114**, 661–665.
2 V. N. Makhov, N. M. Khaidukov, D. Lo, J. C. Krupa, M. Kirm and E. Negodin, *Opt. Mater.*, 2005, **27**(6), 1131–1137.
3 H. Vrielinck, I. Izeddin, V. Y. Ivanov, T. Gregorkiewicz, F. Callens, D. S. Lee, A. J. Steckl and N. M. Khaidukov, *MRS Symp. Proc.*, 2005, **866**, 13–24.
4 H. Vrielinck, F. Loncke, F. Callens, P. Matthys and N. M. Khaidukov, *Phys. Rev. B: Condens. Matter Mater. Phys.*, 2004, **70**, 144111.
5 E. Fargin, B. Lestienne and J. M. Dance, *Solid State Commun.*, 1990, **75**, 769–771.
6 H. N. Bordallo, R. W. Henning, L. P. Sosman, R. J. M. da Fonseca, A. Dias Tavares, Jr, K. M. Hanif and G. F. Strouse, *J. Chem. Phys.*, 2001, **115**(9), 4300.
7 H. N. Bordallo, X. Wang, K. M. Anif, G. F. Strouse, R. J. M. da Fonseca, L. P. Sosman and A. Dias Tavares, Jr, *J. Phys.: Condens. Matter*, 2002, **14**, 12383–12389.
8 A. Vedrine, J. P. Besse, G. Baud and M. Capestan, *Rev. Chim. Miner.*, 1970, **7**, 593.
9 M. V. Korzhik, M. G. Livshits, M. L. Meilman, B. I. Minkov and V. B. Mavlenko, *Opt. Spektrosk.*, 1991, **70**(4), 808–810.
10 Yu. P. Gnatenko, A. O. Borshch, N. Kukhtarev, T. Kukhtareva, I. O. Faryna, V. I. Volkov, P. M. Bukivskij, R. V. Gamernyk, V. I. Rudenko, S. Yu. Paranchych and L. D. Paranchych, *J. Appl. Phys.*, 2003, **94**(8), 4896–4903.
11 M. Cao, J. Jiang, H. Liu and J. Yuan, *Phys. B*, 2005, **364**, 150–156.
12 (*a*) O. Vahtras, O. Loboda, B. Minaev, H. Agren and K. Ruud, *Chem. Phys.*, 2002, **279**, 133–141; (*b*) F. Neese, *J. Am. Chem. Soc.*, 2006, **128**, 10213–10222.
13 (*a*) Z. Y. Yang, C. Rudowicz and J. Qin, *Phys. B*, 2002, **318**(2–3), 188–197; (*b*) W. C. Zheng, Q. Zhou, Y. Mei and X. X. Wu, *Opt. Mater.*, 2004, **27**(3), 449–451; (*c*) D. J. Keeble, M. Loyo-Menoyo, Y. Furukawa and K. Kitamura, *Phys. Rev. B: Condens. Matter Mater. Phys.*, 2005, **71**(22), 224111; (*d*) C. Rudowicz, M. G. Brik, N. M. Avram, Y. Y. Yeung and P. Gnutek, *J. Phys.: Condens. Matter*, 2006, **18**(22), 5221–5234; (*e*) W. C. Zheng, Q. Zhou, X. X. Wu and Y. Mei, *Z. Naturforsch., A: Phys. Sci.*, 2006, **61**(5–6), 286–288; (*f*) S. Y. Wu and H. N. Dong, *J. Lumin.*, 2006, **199**, 517–521; (*g*) M. G. Brik, C. N. Avram and N. M. Avram, *Phys. B*, 2006, **384**(1–2), 78–81.
14 (*a*) T. T. Petrenko, T. L. Petrenko, V. Y. Bratus and J. L. Monge, *Appl. Surf. Science*, 2001, **184**(1–4), 273–277; (*b*) O. V. Yazyev, L. Helm, V. G. Malkin and O. L. Malkina, *J. Phys. Chem. A*, 2005, **109**(48), 10997–11005.
15 C. Rudowicz, *J. Phys.: Condens. Matter*, 2000, **12**, L417–L423.
16 S. Stoll and A. Schweiger, *J. Magn. Reson.*, 2006, **178**(1), 42–55.
17 A. Abragam and B. Bleaney, in *Electron Paramagnetic Resonance of Transition Ions*, Clarendon Press, Oxford, 1970.
18 C. Rudowicz, *J. Phys. C: Solid State Phys.*, 1985, **18**, 1415–1430.
19 Th. Pawlik, J. M. Spaeth, M. Otte and H. Overhof, *Radiat. Eff. Defects Solids*, 1995, **135**, 49–54.
20 D. C. Stjern and R. C. DuVarney, *Phys. Rev. B: Solid State*, 1974, **10**(3), 1044–1051.
21 J. A. Aramburu, J. I. Paredes, M. T. Barriuso and M. Moreno, *Phys. Rev. B: Condens. Matter Mater. Phys.*, 2000, **61**(10), 6525–6534.
22 (*a*) J. M. Spaeth and H. Overhof, *in Point Defects in Semiconductors and Insulators*, Springer, Heidelberg, 2002; (*b*) H. Vrielinck, K. Sabbe, F. Callens and P. Matthys, *Phys. Chem. Chem. Phys.*, 2001, **3**, 1709–1716.